Electromagnetic Image of the Limon Verde Fault (North Chile)

Sebastian Tauber, Freie Universität Berlin, FR Geophysik
email: stauber@zedat.fu–berlin.de

Introduction

To study the electromagnetic response of a fault a dense AMT profile was carried out during a field campaign in 1995 in northern Chile. The profile crosses two faults, but because of limited access only the Limon Verde fault was examined in more detail. The study area is located 30 km south of the mining town Calama, close to Chuquicamata, one of the world largest copper mines.
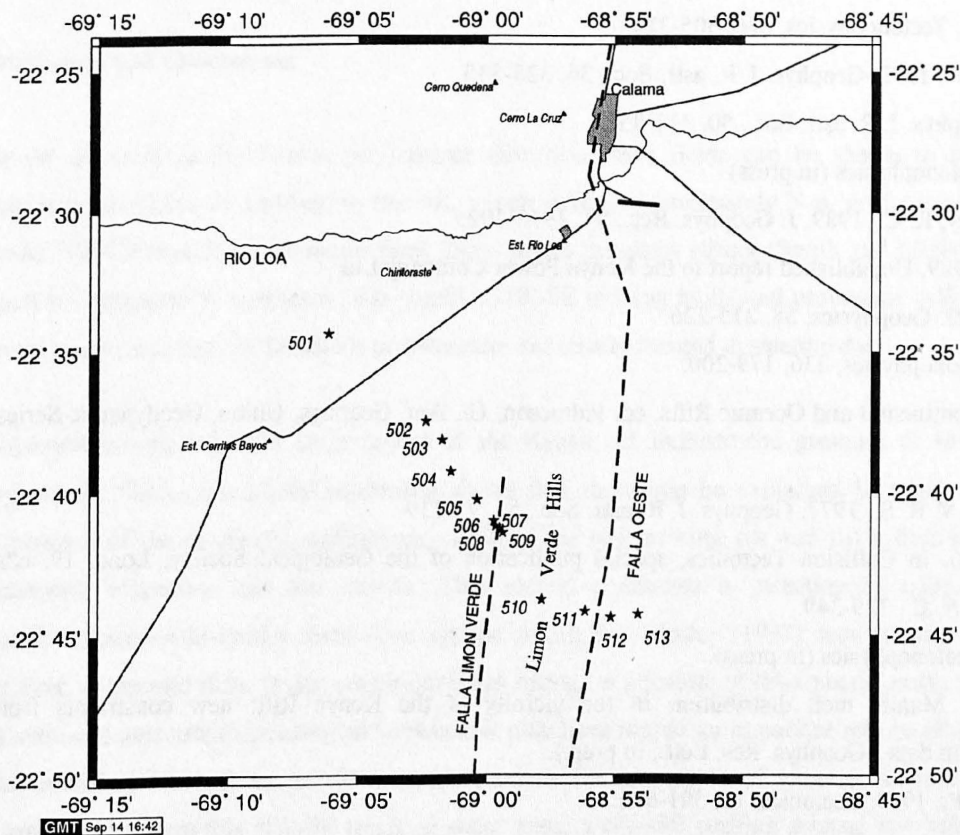

Figure 1: Site locations (asterisk) of the Limon Verde experiment near the town Calama, North Chile. Numbers refer to MT sites. Faults are given in dashed, roads in solid lines. The river Loa is signed with a thin solid line.

Geology

The NNE–SSW striking Falla Limon Verde is a branch of the Falla Oeste (West Fissure Fault System), a fault system of regional scale (approx. NS extent: 900 km), with which the main Chilean copper deposits are associated.

Early paleozoic metamorphic rocks west of the Falla Limon Verde are separated by the fault from younger (permian, upper paleozoic) igneous rocks in the east (BAEZA, 1984), constituting the Limon Verde Hills (cf. Fig. 1). Though the amount of displacement along the Falla Limon

Verde is uncertain, it must have been enormous because 200 Ma of deposits are missing between both units.

The fault is clearly marked by a depression on the western flanks of the Limon Verde hills, but their extent at depth is unknown. The eastern and western foreland of the Limon Verde Hills are covered with gravels and alluvial sediments. The contact of the sedimentary and crystalline rocks strikes nearly parallel to the Falla Limon Verde and Falla Oeste.

Instrumentation and Field–Setup

The instruments used are broadband induction coil magnetometers equipped with two types of recording systems. PDAS (Teledyne) data logger are used to cover the low frequency range from 25 Hz to 0.003 Hz; data are sampled at 20 Hz and 100 Hz. Up to ten PDAS data loggers were running simultaneously in the field. Remote reference technique could be applied, because of GPS time synchronisation.
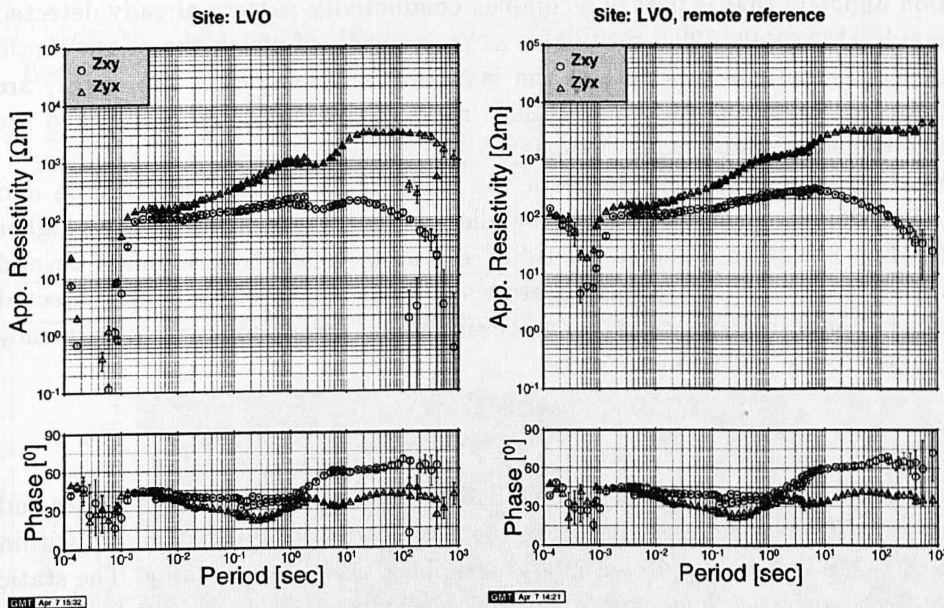

Figure 2: Improvement of estimated apparent resistivity by the use of remote reference technique, displayed for site 509. Left: single site robust processing, right: robust processing with remote reference.

At high frequencies an AMT real–time system (Metronix) was operated in the frequency range from 0.01 Hz to 8000 Hz. To enable remote reference processing technique at high frequencies too, the AMT system was modified to record additionally local magnetic fields in a distance of 300 m remote of the MT site.

The site separation is 300 m within the fault zone and has been expanded to both ends of the profile. The reference site 501 is situated 20 km remote of the survey centre (Fig. 1).

Processing and Interpretation

Robust remote reference processing (EGBERT & BOOKER, 1986; EGBERT, 1989) minimises the effect of random noise in the magnetic fields that can strongly bias the apparent resistivities. Fig. 2 shows the comparison of single site and remote reference processing. The drop of apparent resistivities to the ends of the curve and in the low excitation band $1 - 0.1$ Hz is reduced.

In Figure 4 Bostick pseudosections for E– and B–polarisation are shown. It is obvious that strong static shift effects, especially in the B–polarisation data, are present. An unconstrained Groom&Bailey analysis (GROOM & BAILEY, 1989) reveals that at high frequencies (f > 1 Hz) the distortion parameters are rather small and frequency independent, i.e. twist and shear are ranging between ±12° (cf. Fig. 5, Fig. 6). This is in accordance with the small skew values at higher frequencies (cf. Fig. 7). The Swift angles (Fig. 8) at these frequencies are ±18°, indicating a roughly NS strike direction.

With decreasing frequency (f < 1 Hz) the values of twist and shear increase and get frequency dependent, like the values of the skew, whereas the rotation angles vary considerably. A 2–D interpretation for the lower frequency part of the Limon Verde data set doesn't seem to be appropriate. In opposition to the constrains for a Groom&Bailey analysis we can expect an almost 2–D local structure, striking about NS, embedded in a regional 3–D structure.

This interpretation is highly encouraged by the geomagnetic deep sounding data (GDS). The induction arrows at the period of 400 s (Fig. 9 top, left) are indicating a semi–regional EW striking induction anomaly that is part of a complex conductivity pattern already detected by previous experiments (MASSOW, 1994; SCHWARZ ET AL., 1986), of which the origin is still unknown. Towards shorter periods (about 1 s) the induction arrows (Fig. 9 top, right) are reflecting the resistivity contrast between the crystalline rocks of the Limon Verde hills and the sedimentary fillings of the eastern and western foreland.

Since the electrical strike almost coincides with the strike of the Falla Limon Verde and the Falla Oeste, the individual response of both anomalies can hardly be separated. At higher frequencies (100 Hz) (Fig. 9 bottom, left) we get rid of any other conducting anomaly beyond of the fault zones itself, represented by induction arrows on both flanks of the faults directed oppositely to each other. Fig. 9 (bottom, right) shows the induction arrows at the same frequency in some more detail close to the Falla Limon Verde.

Modelling

The conductivity model shown in Figure 3 was derived by an Occam 2–D inversion of phases and apparent resistivities of both polarisations. The data that are used for the inversion are within the frequency range of 1–220 Hz and calculated in a geographical co–ordinate frame. The static shift factors are also obtained by the inversion, under the constraint that static shift factors for E– and B–polarisation sum up to zero. This is not already justified by the data because there is more downward then upward shift (cf. 4, but this is of minor effect to the resulting model. The comparison of the modelled and observed phases is presented in Figure 10 and 11 show that there is a good fit of modelled and observed data. The RMS–misfit after the 25th iteration is 1.71.

Conclusion

2–D Occam inversion of apparent resistivities and phases give no evidence for an enhanced conductivity associated with Limon Verde fault. On the contrary towards greater depth the fault seems to be more resistive in respect to the surrounding medium. Whereas high frequency induction arrows indicate the fault as a shallow and very narrow zone of increased conductivity. The differences in the MT and GDS results can be explained by the way the sensors are installed. Magnetic variations are recorded at a fixed location by one vertical induction coil, whereas telluric recordings are averaging the electric field along a finite dipole length. The Limon Verde fault is only noticed by scattering effects and is too narrow to be resolved by broadband MT data.

References

L. BAEZA, 1984: *Petrography and tectonics of the plutonic and metamorphic complexes of Limón Verde and Mejillones Peninsula, Northern Chile.* Dissertation, Eberhard-Karls-Univ. Tübingen.

G. D. EGBERT, 1989: Multivariate analysis of geomagnetic array data II random source models. *J. Geophys. Res.*, **94**(B10):14249–15162.

G. D. EGBERT & J. R. BOOKER, 1986: Robust estimation of geomagnetic transfer functions. *Geophys. J. R. astr. Soc.*, **87**:173–194.

R. W. GROOM & R. C. BAILEY, 1989: Decomposition of Magnetotelluric Impedance Tensors in Presence of Local Three-Dimensional Galvanic Distortion. *J. Geophys. Res.*, **94**(B2):1913–1925.

W. MASSOW, 1994: *Magnetotellurik in der Westkordillere Nordchiles.* Diplomarbeit, Freie Univ. Berlin.

G. SCHWARZ, E. MARTINEZ & J. BANNISTER, 1986: Untersuchungen zur elektrischen Leitfähigkeit in den zentralen Anden. *Berliner geowiss. Abh.*, **A66**:49–72.
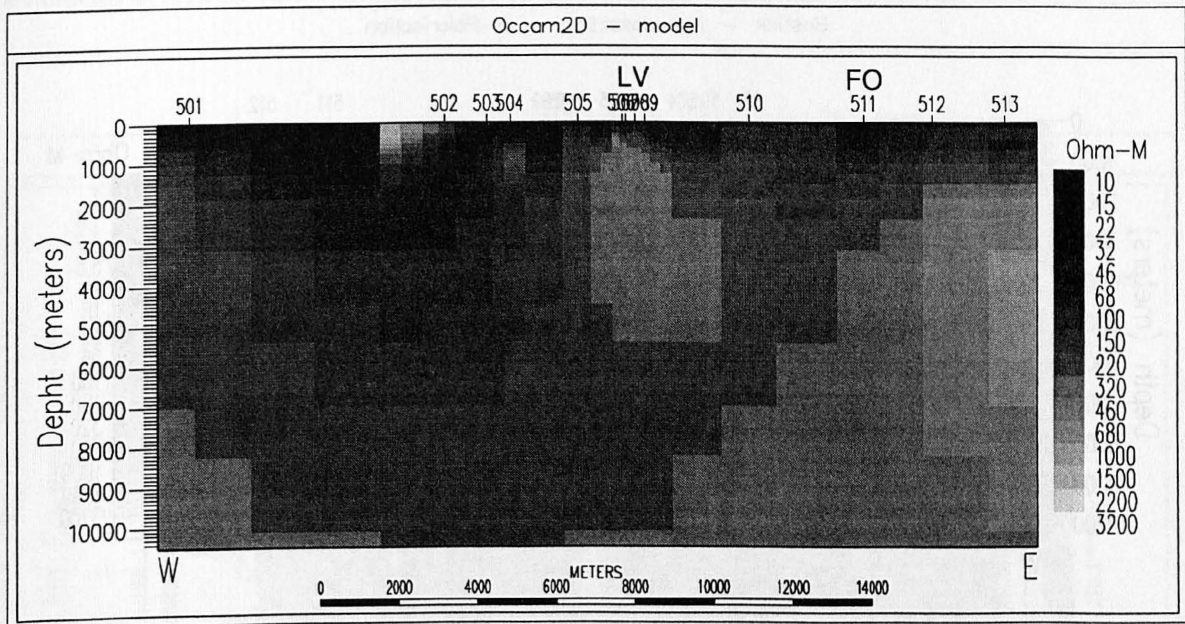
Figure 3: 2–D conductivity model obtained by an Occam inversion of phases and apparent resistivities of both polarisations. The model displayed is the result of the 25th iteration. The achieved RMS–misfit is 1.28. LV = Falla Limon Verde, FO = Falla Oeste.
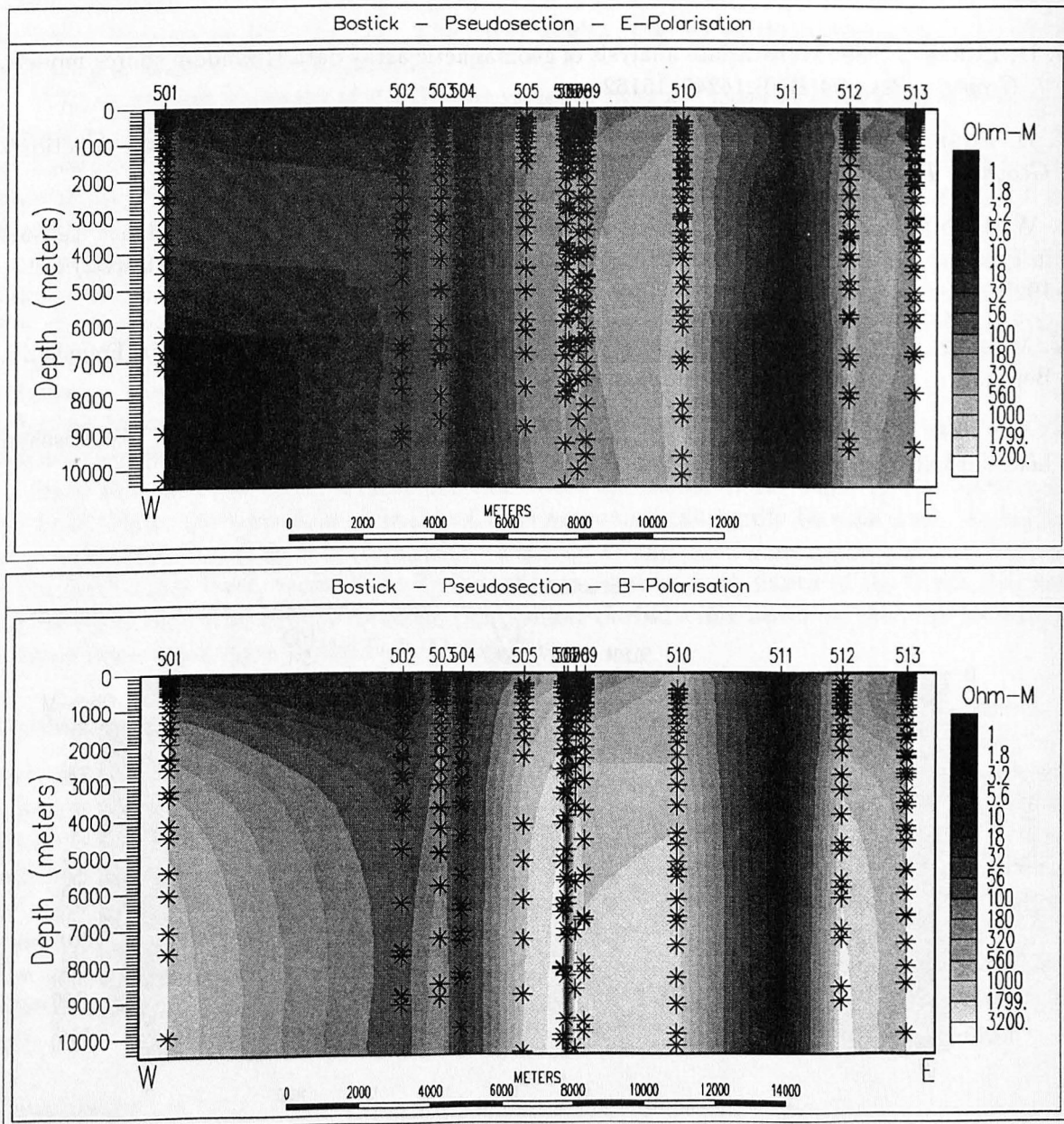
Figure 4: The Bostick pseudosections of E– and B–polarisation display strong static shift effects. At Site 511, located close to the fault Falla Oeste, both polarisations are strongly downward shifted, whereas at site 507 at the edge of the Limon Verde fault only the B–polarisation is effected. (Black asterisk within the pseudosections indicate frequencies where observed data are present.)
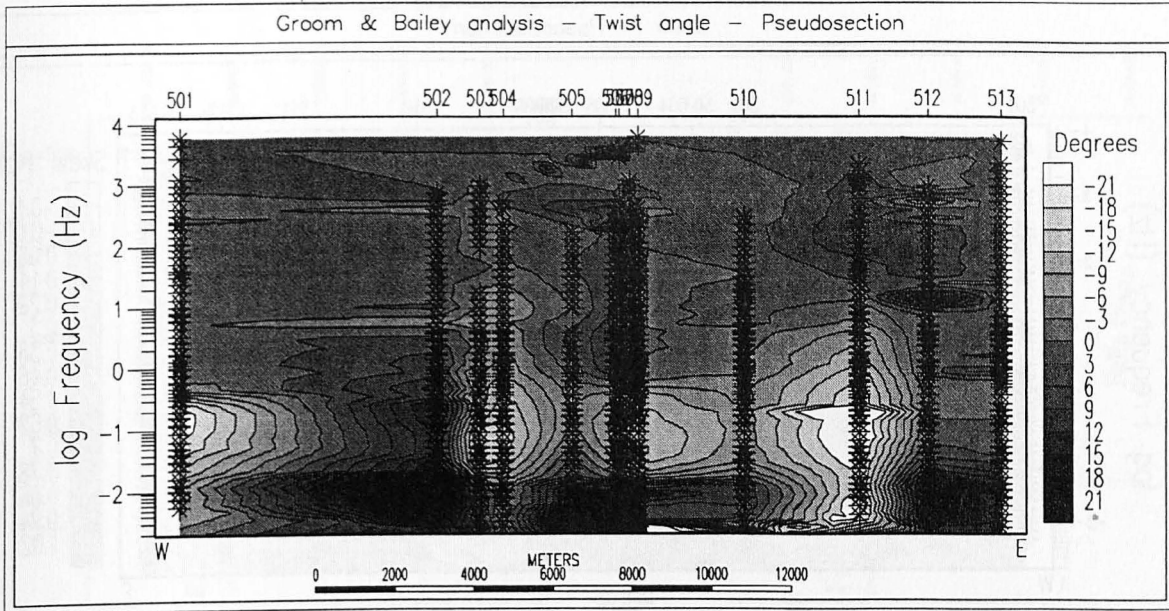
Figure 5: Pseudosection of twist angles obtained by an unconstrained Groom&Bailey analysis. At high frequencies the twist values are small and nearly frequency independent. Towards lower frequencies the twist varies considerably. (Black asterisk ... see caption of figure 4)
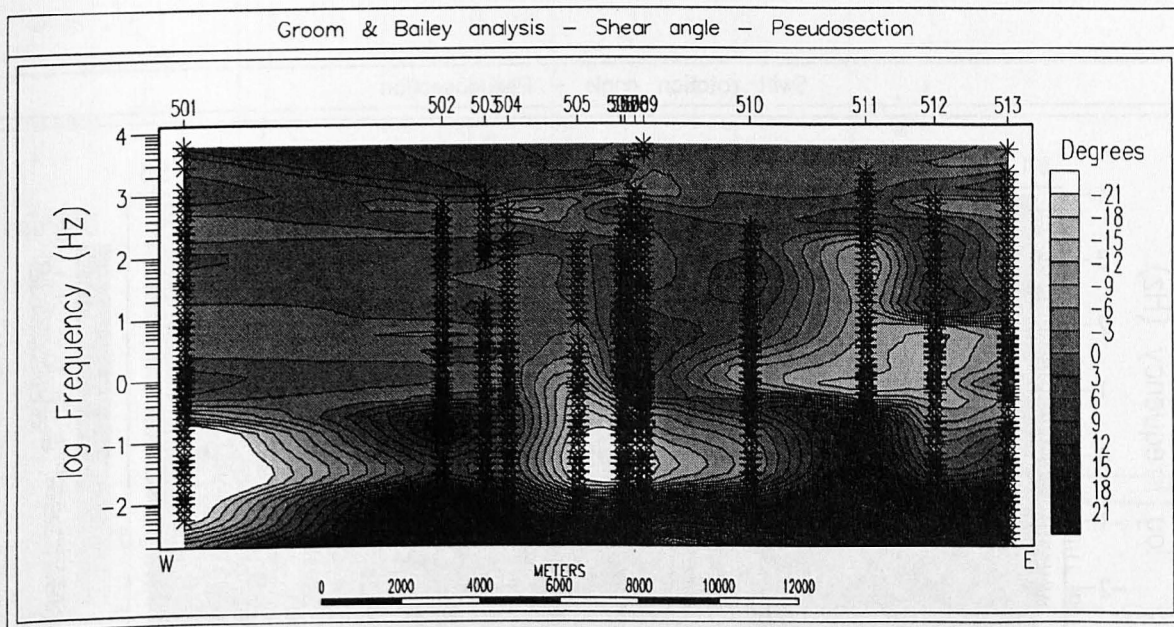

Figure 6: Pseudosection of shear angles obtained by an unconstrained Groom&Bailey analysis. Apart from some superficial structures which are artefacts of the interpolation and not represented by data (black asterisk), the shear angles at high frequencies are reasonable small and nearly frequency independent. Like the twist angles the shear angles increase with decreasing frequencies.
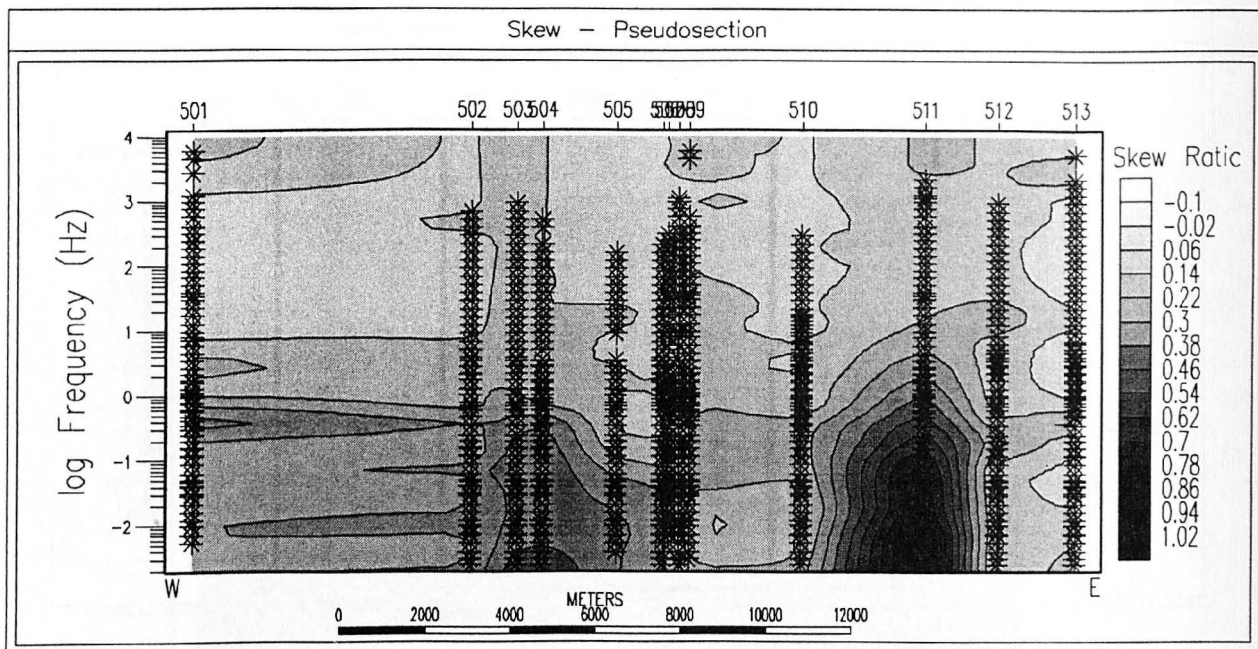
Figure 7: The skew pseudosection show very low skew values (less then 0.22) for the high frequency range indicating a roughly 2–D resistivity structure for shallow depth. Nevertheless site 511 can't be treated as simple 2–D, even in the high frequency range because of the large shear and twist values (cf. Fig. 5, Fig. 6). (Black asterisk ... see caption of figure 4)
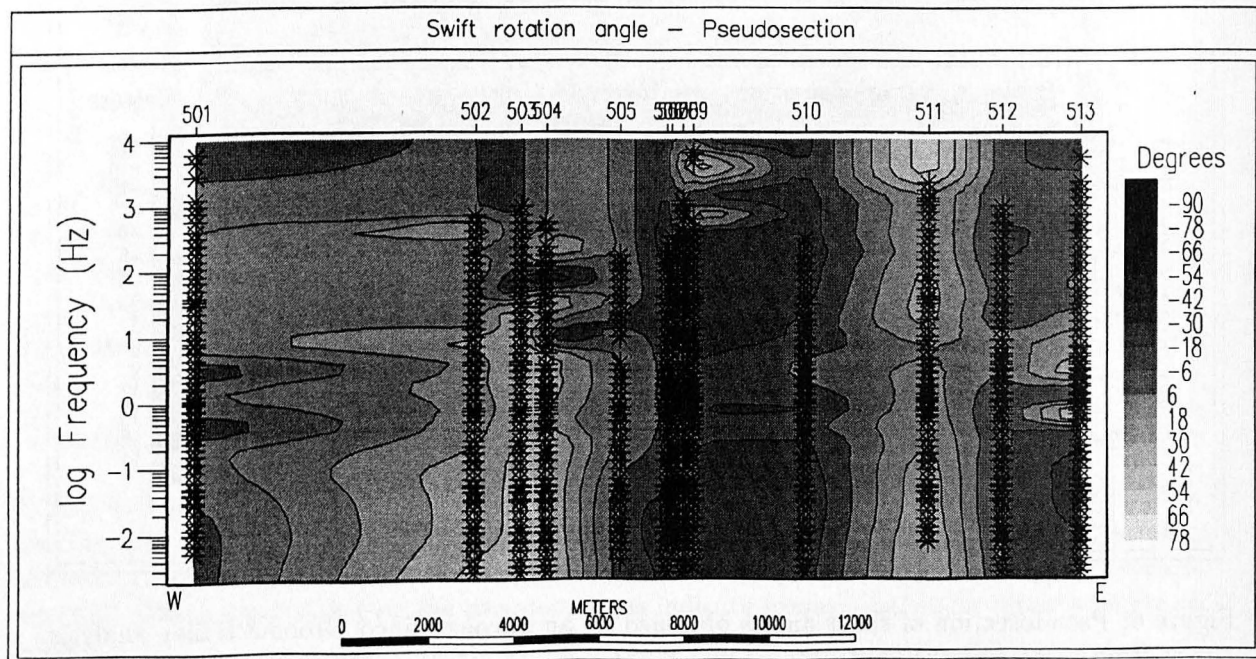

Figure 8: Pseudosection of swift rotation angle. The rotation angles in the high frequency range vary between ±18° (except of site 511) indicating a roughly NS strike direction. (Black asterisk ... see caption of figure 4)
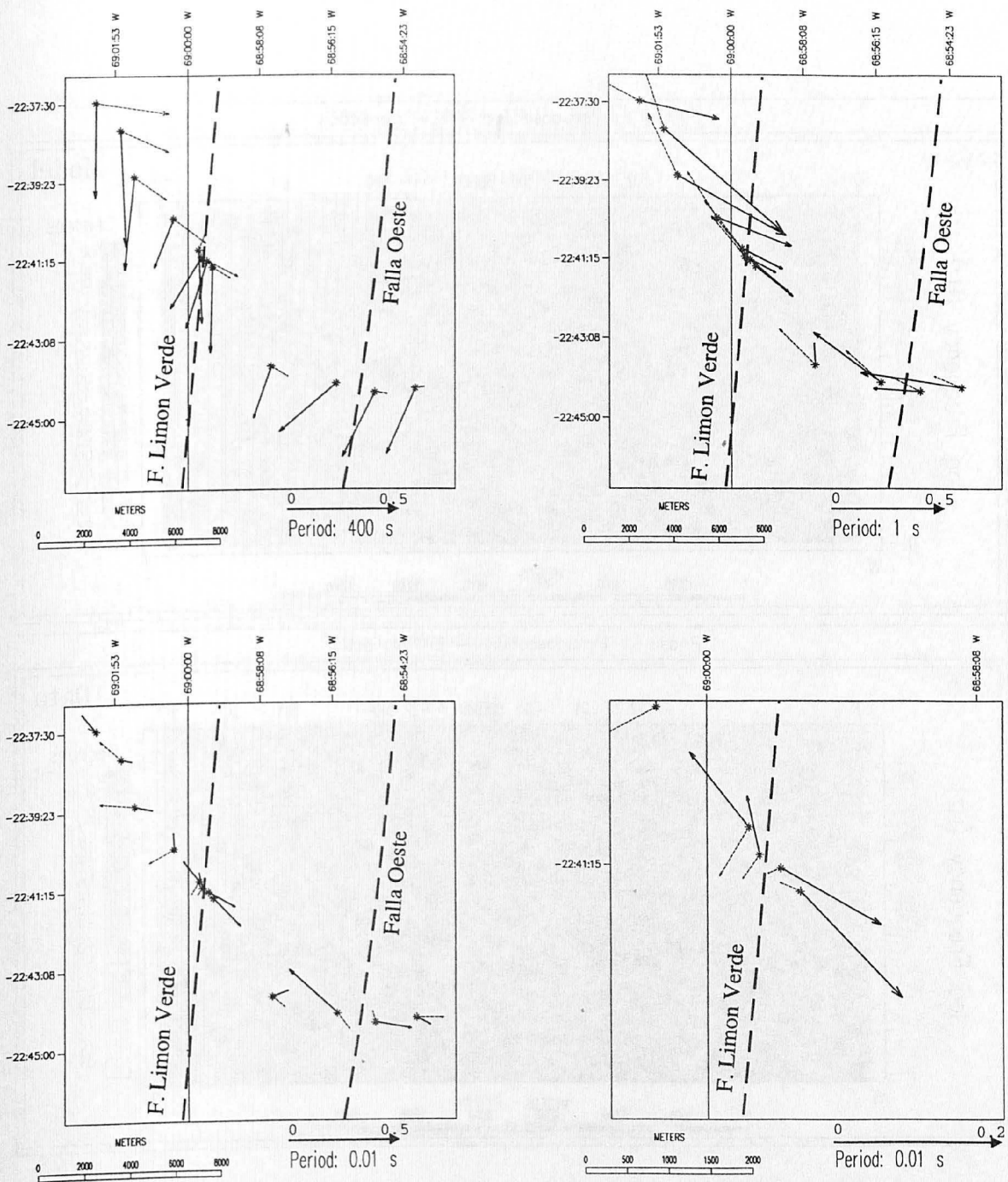
Figure 9: Induction arrows in plan view for different periods. Real arrows (Schmucker convention) with hat, imaginary arrows without hat. Dashed lines mark faults. Top, left: at 400 s, the induction arrows indicating an regional EW striking resistivity anomaly. Top, right: the induction arrows at 1 s pointing to the crystalline rocks (Limon Verde Hills) in between the Falla Limon Verde and the Falla Oeste. Bottom, left: the induction arrows at 0.01 s are directed oppositely on both sides of the faults. Bottom, right: enlargement of the induction arrow pattern at 0.01 s close to the Falla Limon Verde.
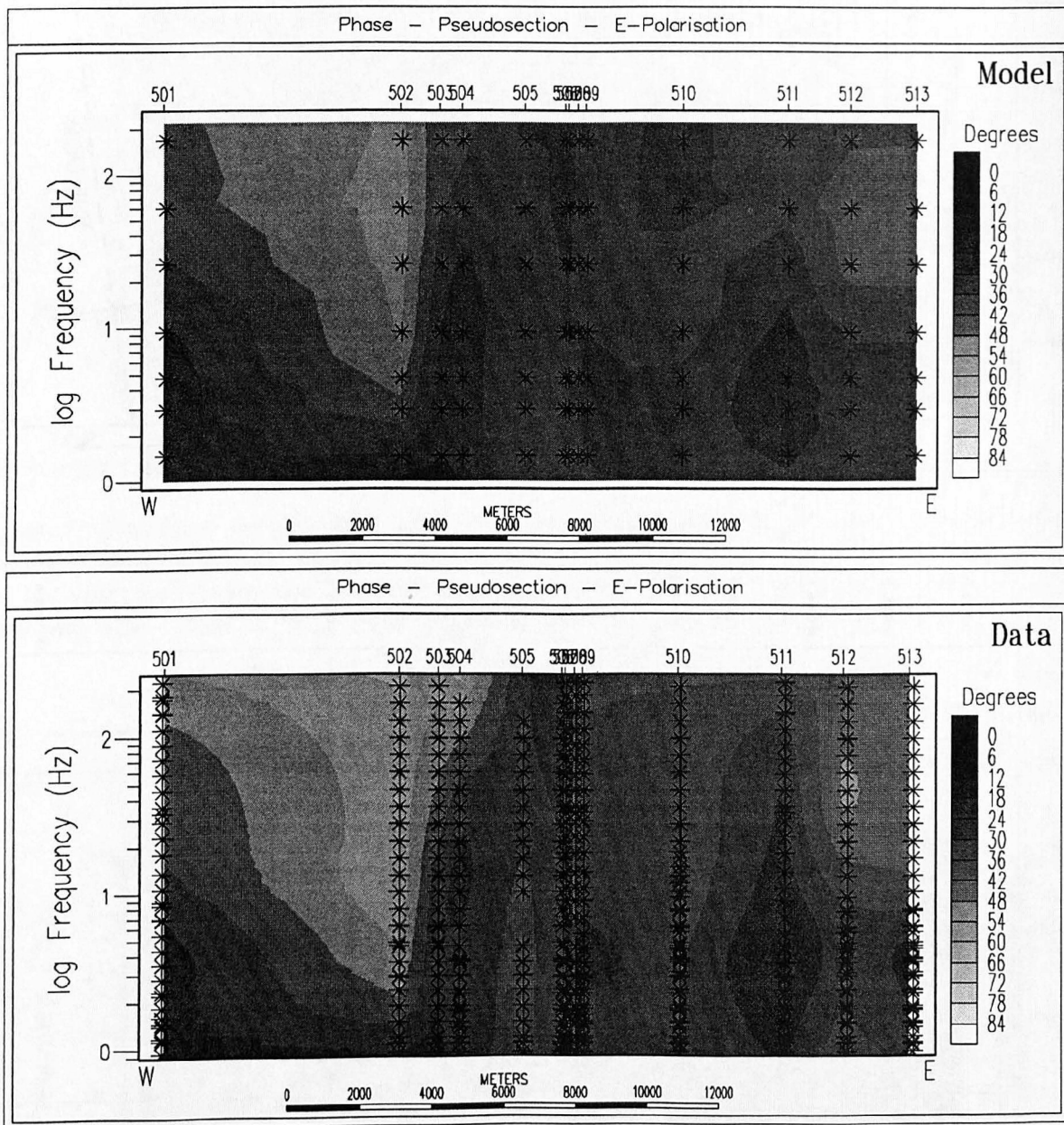
Figure 10: Comparison of modelled and observed phases of E-polarisation. Top: Phase pseudosection of model response. Black asterisk indicate frequencies of data which were considered by the inversion. Bottom: Phase pseudosection of observed data in the frequency range of 1–220 Hz. Black asterisk within the pseudosection indicate frequencies where observed data are present.

Figure 11: Comparison of modelled and observed phases of B–polarisation. Top: Phase pseudosection of model response. Black asterisk indicate frequencies of data which were considered by the inversion. Bottom: Phase pseudosection of observed data in the frequency range of 1–220 Hz. Black asterisk within the pseudosection indicate frequencies where observed data are present.